Heliyon 8 (2022) e10663

Contents lists available at ScienceDirect

Heliyon

journal homepage: www.cell.com/heliyon

Research article

Fabrication of strong bioresorbable composites from electroexplosive Fe-Fe_3O_4 nanoparticles by isostatic pressing followed by vacuum sintering

A.S. Lozhkomoev [a,*], S.O. Kazantsev [a], O.V. Bakina [a], A.V. Pervikov [a], A.F. Sharipova [b], A.V. Chymaevskii [a], M.I. Lerner [a]

[a] Institute of Strength Physics and Materials Science of the Siberian Branch of the Russian Academy of Sciences, ISPMS SB RAS, 634021 Tomsk, Russia
[b] Department of Materials Science and Engineering, Technion, 3200003 Haifa, Israel

ARTICLE INFO

Keywords:
Fe-Fe_3O_4 nanopowders
Electrical explosion of wire
Bioresorbable composites
Sintering
Corrosion
Strength

ABSTRACT

Bulk samples with high mechanical strength reaching 1000 MPa were obtained from electroexplosive Fe-Fe_3O_4 nanoparticles containing 81 wt. % Fe. Maximum strength is achieved by consolidation of the nanoparticles by isostatic pressing followed by vacuum sintering at 700 °C. A further increase in the sintering temperature leads to the formation of large pores with a size of up to 5 μm and an intense interaction of Fe and Fe_3O_4 with the formation of FeO leading to the embrittlement of the samples and a decrease in their strength. The degradation rate of Fe- Fe_3O_4 samples in NaCl (0.9% wt.) and Hank's solution is 7 times higher than that of samples obtained by sintering an electroexplosive Fe nanopowder under the same conditions.

1. Introduction

Iron-based biodegradable materials are promising candidates for orthopedic implants intended for load bearing bones [1, 2]. The prospects for the use of these materials are due to their high strength: from 400 MPa, for pure iron [3, 4] and up to 1550 MPa, for an iron-based alloy Fe-10Mn-1Pd [5]. The main disadvantage of currently used materials based on iron is their low rate corrosion in a biological environment [5, 6, 7]. This problem can be solved by applying iron-based alloys or adding fine particles of noble metals to alloys [7]. Such particles, being cathodes with respect to iron, induce microgalvanic corrosion and promote active damage of the iron matrix. For example, the Fe-35Mn alloy (35 wt% Mn) has a higher corrosion rate compared to pure iron - 0.44 mm/year versus 0.2 mm/year, respectively [7]. Also, using the Fe-10Mn alloy as an example, it was demonstrated that its alloying with 1 wt% Pd led to a significant increase in the degradation rate of the iron matrix [5]. The efficiency of this approach can be enhanced by reducing the particle size of the noble metal to the nanoscale and obtaining its homogeneous distribution in the matrix.

For the manufacture of biodegradable iron based materials, as a rule, methods of conventional metallurgy are used [8]. The manufacturing methods affect the microstructure, mechanical properties as well as the biodegradation rate [9].

Bioresorbable alloy Fe-30Mn [10], obtained by casting followed by forging, exhibited relatively low mechanical properties: yield strength 242 MPa and ultimate strength - 632 MPa. The Fe30Mn6Si alloy obtained by casting [11] has been shown to consist of martensite and austenite phases with a smaller grain size and a higher ultimate strength than pure iron obtained by the same method. A series of iron binary alloys (Fe - Mn/Co/Al/W/Sn/B/C/S, the content of all alloying elements about 3 wt %), made by casting followed by rolling, were also investigated [12]. No noticeable effect has been found when alloying with Mn, Co, Al and W, a significant reduction in grain size has been observed with boron, and alloying with Sn sharply reduced the mechanical strength of the Fe30Mn6Si alloy. Alloying with Mn, Co, W, B, C and S increased the yield strength and ultimate strength in rolled alloys: the maximum value of the yield strength was observed in the Fe-W system, 450 MPa, with a tensile strength of 680 MPa. In these materials, the difference between yield strength and tensile strength increased. Only alloying with Co, W, C, and S had a positive effect in terms of both mechanical and corrosion properties. It is believed that alloying with several elements should have a more pronounced effect on the corrosion properties of iron-based alloys.

The Fe-10Mn-1Pd alloy with high mechanical properties was obtained using additional thermomechanical treatments [13]. After casting and quenching, isothermal aging and quenching were applied [14]. A pronounced increase in the yield point to 950 MPa and the ultimate strength to 1550 MPa are due to the formation of lamellar Pd particles,

* Corresponding author.
E-mail address: asl@ispms.tsc.ru (A.S. Lozhkomoev).

https://doi.org/10.1016/j.heliyon.2022.e10663
Received 12 January 2022; Received in revised form 16 May 2022; Accepted 9 September 2022

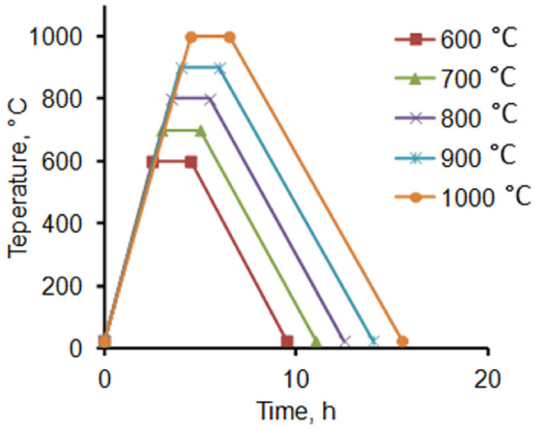

Figure 1. Sintering mode of Fe - Fe_3O_4 nanopowder.

coherent to the <100> planes of the iron matrix, separated during aging. The study of the effect of Pd particles was carried out on systems containing 10 wt% Mn, with different content of Pd (1, 3 and 6 wt%).

The average grain size of pure iron material obtained by plasma-spark sintering was determined to be about 35 μm [15], which is 3–4 times less than that of pure iron material obtained by casting. Alloying with carbon nanotubes (0.5 and 1 wt%) and W (2 and 5 wt%) reduced the iron grain size on average to 20 and 18 μm, respectively. Nevertheless, such a thinning of the structure had practically no effect on the yield strength and corrosion properties of the alloys. A significant improvement in properties of the material with a similar structure (average grain size is about 25–34 μm, depending on the material composition) was obtained on composites Fe - Fe_2O_3 (2–50 wt% Fe_2O_3) prepared by the spark plasma sintering (SPS) method [16]. The corrosion rate of the Fe-5Fe_2O_3 composite was 14 times higher due to the electrochemical reaction, where Fe_2O_3 acted as the cathode, and the yield point was 2 times higher in comparison with iron cast material.

Fe - Fe_mO_n nanocomposites were produced from Fe_2O_3 nanopowder by a partial reduction followed by cold sintering. This method has been shown to avoid undesired structural changes such as grain coarsening or accumulation of the reinforcing phase at grain boundaries. The composites obtained had a very dense structure (about 97% of theoretical density) and demonstrated high mechanical strength — the compressive yield strength of 1035 MPa, which is four times higher than that for Fe - 5Fe_2O_3 obtained using SPS [17].

Fe - Fe_3O_4 nanocomposites can be obtained by electrical explosion of a Fe wire (EEW) in an oxygen-containing atmosphere [18]. The formation of nanoparticles during an electrical explosion occurs during rapid condensation of metal vapors, which contributes to the uniform distribution of the phases formed over the bulk of the nanoparticle with small sizes of coherent scattering regions [19, 20]. The manufacture of compact materials from such nanoparticles makes it possible to provide the nanostructured state of the composite, as well as multiple boundaries phase separation Fe - Fe_3O_4, which can contribute to a high rate of electrochemical corrosion during biodegradation in comparison with pure iron materials.

In this work, by the EEW method of a Fe wire in an oxygen-containing atmosphere, Fe - Fe_3O_4 nanopowders with iron content of 81 wt% were obtained, the effect of vacuum heat treatment of compact samples on their structural and physicomechanical properties was studied, and the rate of biodegradation of the obtained composites was evaluated.

2. Experimental

Fe - Fe_3O_4 nanopowders were produced by EEW method using the setup described in details previously [21]. To produce nanoparticles, an iron wire with a diameter of 0.3 mm and a length of 65 mm was exploded by a pulse of current at a voltage of 28.5 kV and a capacitance of 1.6 μF in a mixture of argon and oxygen gases, where the oxygen content was 1.3 vol. % according to the method described in [18]. In this mode, Fe - Fe_3O_4 particles with a core-shell structure are formed, with the iron content being about 81 wt. %.

The prepared nanopowders were characterized by transmission electron microscopy (TEM) using a JEM-2100 electron microscope (JEOL, Tokyo, Japan) integrated with an X-Max energy dispersive spectrometer (Oxford Instruments, Abingdon, UK), and scanning electron microscopy (SEM) using LEO EVO 50 electron microscope (Carl Zeiss AG, Jena, Germany) equipped with an INCA-Energy 450 EDS analyzer (Oxford Instruments, Abingdon, UK).

The phase composition of the nanoparticles and bulk materials were carried out on XRD-6000 diffractometer (Shimadzu, Kyoto, Japan) using CuKα radiation. The data obtained were processed using POWDER CELL 2.4 software package and the PDF 4+ database. The parameters of the fine crystal structure, namely the size of the coherent scattering regions (D_{CSR}), were determined from the Williamson-Hall plots.

The average size of nanoparticles was determined and histograms of the particle size distribution were plotted based on the electron microscopy data. To construct the histogram, the sizes of 850 particles were measured. The average particle size was determined by the expression $a_n = \Sigma n_i a_i / \Sigma n_i$, where n_i is the number of particles with diameter a_i.

To obtain samples of consolidated Fe - Fe_3O_4 nanopowders, the method of isostatic pressing at a pressure of 30 MPa was used, followed by sintering in vacuum (10^{-5} Torr) in the temperature range 600–1000 °C Figure 1 shows a diagram of nanopowder sintering.

The samples were heated from ambient to the targeted temperature at a rate of 3.75°/min, followed by dwelling for 2 hours and cooling down to ambient temperature.

The relative density of the consolidated samples was determined as an averaged value by calculation based on the geometric dimensions, mass and density of the Fe - Fe_3O_4 composite containing 81 wt. % Fe. The measurements in each series were carried out for 5 samples.

The compression tests were performed on a UTS-110 M versatile dual-zone floor machine. The testing was performed on samples carved out of the consolidated sample.

The degradation rate of the consolidated samples was evaluated under static conditions. The samples were immersed in Hanks' Balanced Salt Solution with pH = 7.2 and saline solution (0.9% NaCl), simulating a biological environment under conditions of slow and accelerated degradation, for 30 days. Iron nanopowder samples prepared under similar conditions were used for the control. In accordance with ASTM G31-21, the ratio of the sample surface area to the volume of the biodegradation solution was 1 cm^2 per 50 ml of liquid. The kinetics of biodegradation was assessed by the change in the mass of the samples after the removal of corrosion products and by the amount of iron ions released into the biological environment.

The corrosion rate V (mm/year) during immersion was calculated by the Eq. (1) [22]:

$$V = K(W_0\text{-}W_t)/DAt \quad (1)$$

where $K = 8{,}76 \times 10^4$; W_0 и W_t - mass of samples before and after purification from corrosion products, respectively; A is the surface area exposed to the solution (cm^2); t - exposure time (h), D - material density (g/cm^3).

3. Results and discussion

Figure 2a shows a TEM image of Fe - Fe_3O_4 nanoparticles obtained by electrical explosion of iron wire in an oxygen-containing atmosphere. As can be seen from Figure 2a, the particles predominantly have a core-shell structure. TEM-EDS elemental mapping images (Figure 2b-d) indicate that the particle core consists of iron, while the shell contains oxygen as well. Thus, we can assume that the iron core of the particles is covered by

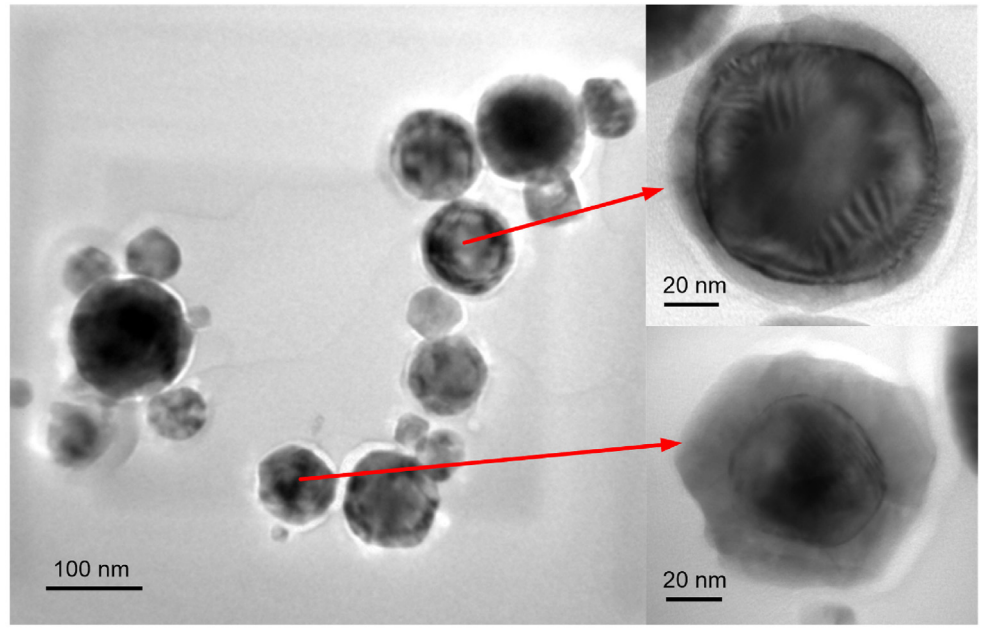

(a)

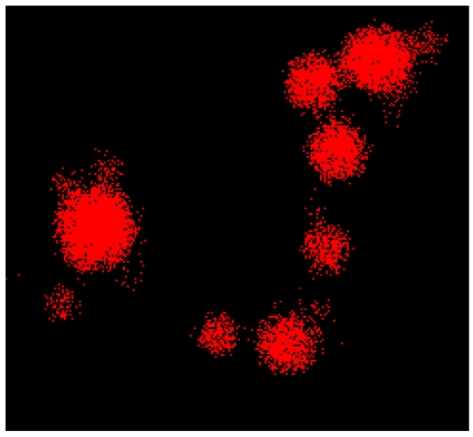

(b)

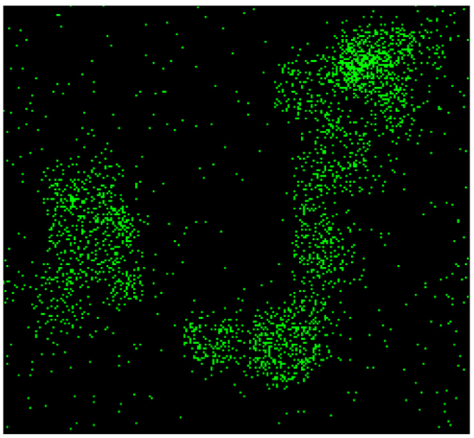

(c)

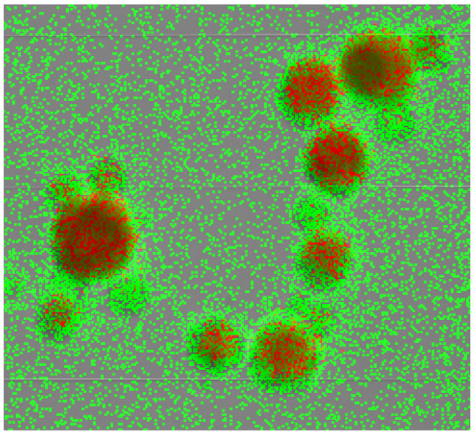

(d)

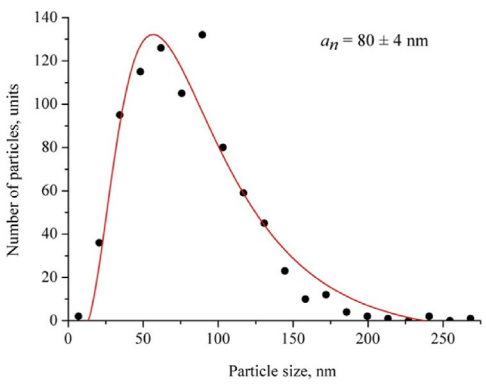

(e)

Figure 2. TEM image (a) and TEM-EDS elemental mapping images of Fe - Fe_3O_4 nanoparticles (b–d): (b) –Fe edge, (c) –O edge, (d) – overlay, (e) - nanoparticle size distribution.

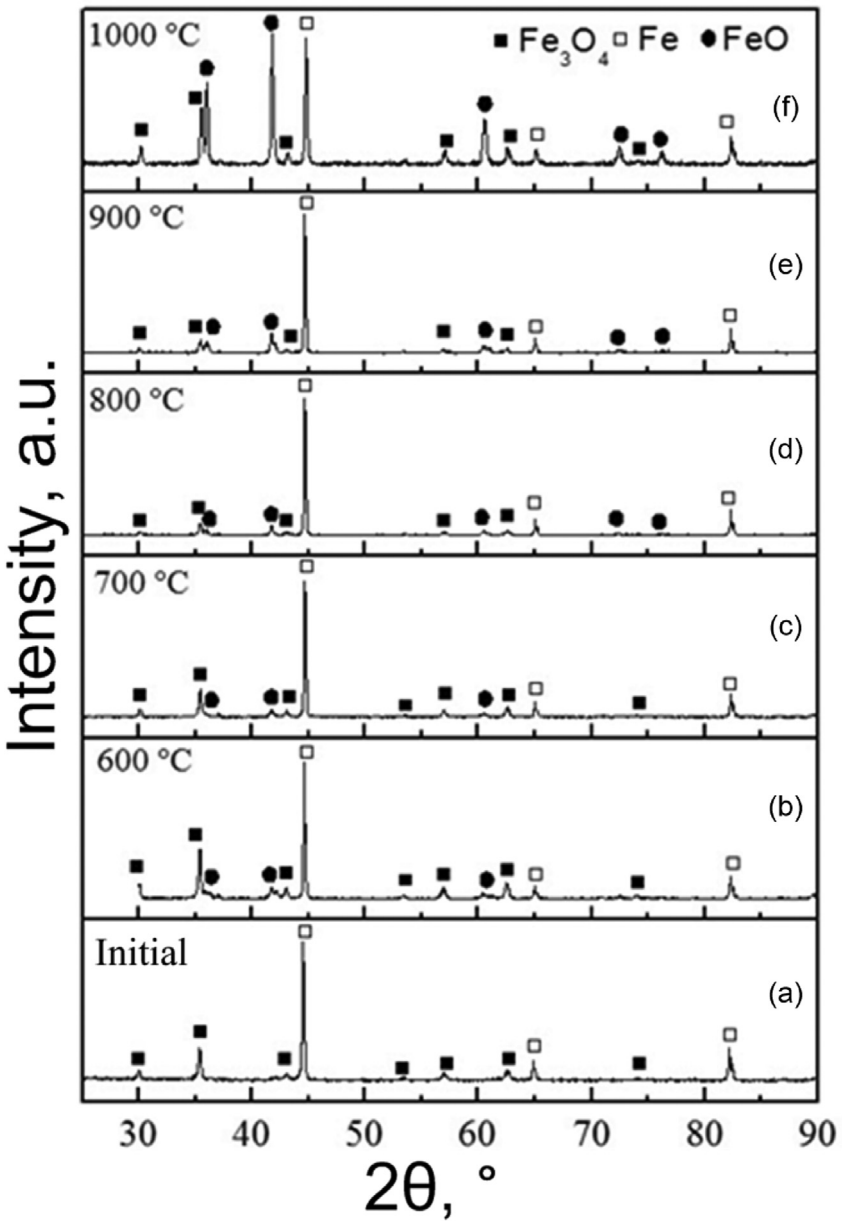

Figure 3. XRD of Fe - Fe_3O_4 nanopowders consolidated by isostatic pressing followed by vacuum sintering. (a) – original sample, (b) – sintered at 600°C; (c) – at 700°C; (d) – at 800°C; (e) – at 900°C; (f) – at 1000°C

an iron oxide shell. The earlier studies of similar particles confirm such structure [18]. The size distribution of nanoparticles is close to the normal-logarithmic variant of the distribution with asymmetry on the right side. The size distribution maximum is located at 80 nm (Figure 2e).

According to XRD data (Figure 3a), the composition of the nanopowder after isostatic pressing is represented by Fe (81 wt%) and Fe_3O_4 (19 wt%) phases. When sintering the samples at a temperature of 600 °C, the FeO phase begins to form (Figure 3b). With an increase in the sintering temperature, the intensity of the FeO peaks increases (Figure 3c-f). A significant increase in the FeO phase content occurs on sintering at 1000 °C (Figure 3f).

The formation of FeO phase is due to the interaction of metallic iron with Fe_3O_4 when heating according to the Eq. (2):

$$Fe + Fe_3O_4 \rightarrow 4FeO \quad (2)$$

Thus, an increase in the sintering temperature of the nanopowders above 800 °C will lead to a decrease in metallic iron content in the samples, which can negatively affect their physico-mechanical characteristics.

An increase in the sintering temperature of the Fe - Fe_3O_4 nanopowders leads to an increase in relative density of the samples to 77% of theoretical density (TD), while the size of the coherent scattering regions (D_{CSR}) of Fe does not change monotonically (Figure 4). When the sample is heated to 600 °C, an increase in D_{CSR} is caused by the redistribution of structural defects. The decrease in D_{CSR} upon heating at 700 °C may be due to Fe recrystallization accompanied by grain fragmentation. Also, in the temperature range 600–700 °C, there is an abrupt increase in the relative density from 65 to 75% of TD which with a further increase in the sintering temperature, increases by only 2%. The increase in D_{CSR} in the temperature range 700–900 °C is probably due to collective

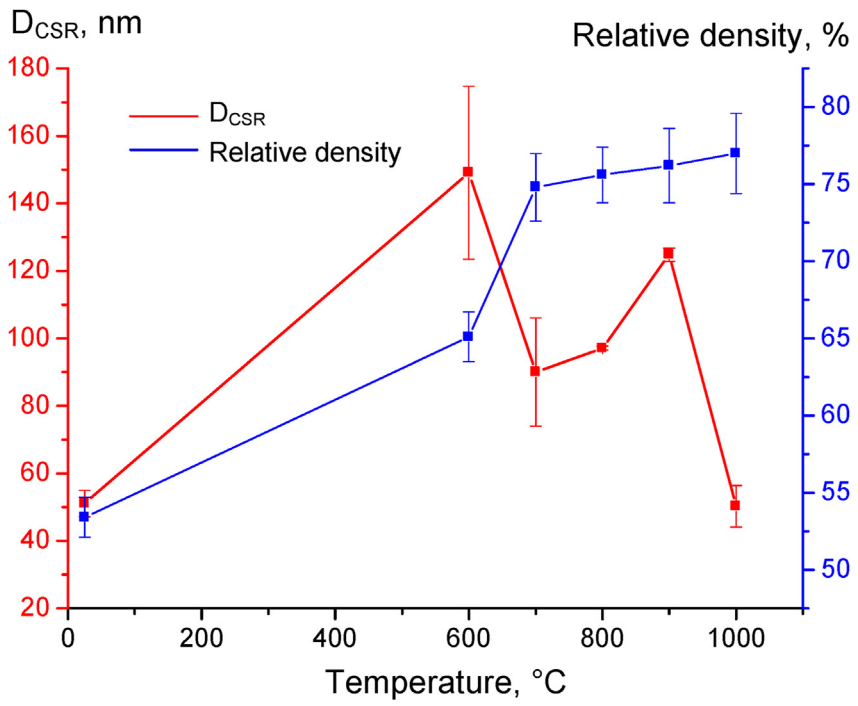

Figure 4. Dependence of D_{CSR} and relative density of consolidated Fe - Fe_3O_4 nanopowders on temperature.

recrystallization, accompanied by a decrease in the length of the crystallite boundaries. A sharp decrease in the D_{CSR} of Fe at 1000 °C can be associated with the intense interaction of Fe with Fe_3O_4 which leads to the appearance of structural defects caused by the diffusion of oxygen into the Fe crystal lattice.

Using SEM technique, the surface of a compact sample obtained by sintering at 600 °C (Figure 5 a) has been found to be represented by a set of iron-enriched particles ranging in size from 100 nm to 10 μm (light areas), which are distributed in a phase enriched iron oxide (dark area). The surface of the sample is characterized by the presence of a large number of pores with a size of 0.1–3 microns. The sample sintering occurs in the temperature range 600–700 °C, resulting in a marked increase in the density of the sample. Particles enriched with iron are observed, both near spherical and irregularly shaped, which may indicate the coalescence of small particles (Figure 5 b). In the sintering temperature range lying between 800 - 900 °C, the coalescence processes intensify, which leads to the appearance and increase of irregularly shaped regions enriched in the Fe or Fe_3O_4 phases (Figure 5 c, d). In this case, the sample obtained at 900 °C is characterized by the appearance of pores, which could have formed due to the combination of small particles into larger aggregates (Figure 5 d). A large number of pores with a size of 0.5–5 microns appear upon heat treatment of the sample at 1000 °C. In this case, the area of the regions enriched in Fe is noticeably reduced due to the appearance of the FeO phase as a result of the interaction of Fe and Fe_3O_4 (Figure 5 e).

Compressive stress – strain curves were plotted for the samples obtained by isostatic pressing followed by sintering in vacuum (Figure 6). As is seen in Figure 6, the highest tensile strength, about 1000 MPa, is observed for the sample sintered at 700 °C, which is slightly less than that for the sample cold sintered from iron nanoparticles with an average size of 30 nm [23]. Samples sintered at 800 °C show appreciable plastic deformation, but the tensile strength is lower and is about 900 MPa. This is due to more effective sintering of the powder at this temperature, which is also confirmed by SEM data (Figure 5). Brittle fracture is characteristic for the samples obtained by sintering at 900 °C and 1000 °C, the ultimate strength being 580 and 600 MPa, respectively.

The results obtained showed that this method can be used to prepare sufficiently strong samples comparable in strength to the Fe - Fe_mO_n composites prepared by cold sintering [17]. At the same time, the relative density of the prepared samples is about 75% of TD, which can be used to fill the existing pores with various drugs, for example, to ensure the antimicrobial activity of the implant or to stimulate osseointegration. The most pronounced strength characteristics are exhibited by the samples obtained at 700 °C, which is due to the onset of coalescence of nanoparticles with a decrease in the CSR size and the absence of intense interaction of Fe with Fe_3O_4 at a given temperature, which is observed at 900 °C and above.

The degradation rate in saline solution was evaluated for the sample obtained at 700 °C. For comparison, bulk samples obtained under the same conditions from Fe nanoparticles were also tested. The relative change in the mass of the samples under study as a function of the degradation time is shown in Figure 7.

The weight loss of Fe-Fe_3O_4 samples has proved to be significantly higher than that of Fe samples both in saline solution and in Hank's solution being 16% and 12%, respectively. The weight loss of iron samples in saline solution and in Hank's solution was 2% and 0.9%, respectively. The degradation rates in terms of weight loss after 30 days of exposure in a normal saline were for Fe-Fe_3O_4 samples – 12.5 $g\times m^{-2}\times day^{-1}$, for Fe – 1.7 $g\times m^{-2}\times day^{-1}$ or 0.62 mm/year and 0.08 mm/year, respectively. Sample Fe-Fe_3O_4 exhibited a relative big degradation rate comparable to Mg-based composite fabricated via laser additive manufacturing with degradation rate 0.89 mm/year [24]. Thus, the presence of nano-galvanic pairs Fe-Fe_3O_4 increased the corrosion rate of the samples by a factor of 7 compared to pure Fe.

Figure 8 shows diagrams of iron ion concentration changes released into Hank's solution at different immersion durations. An increase in the

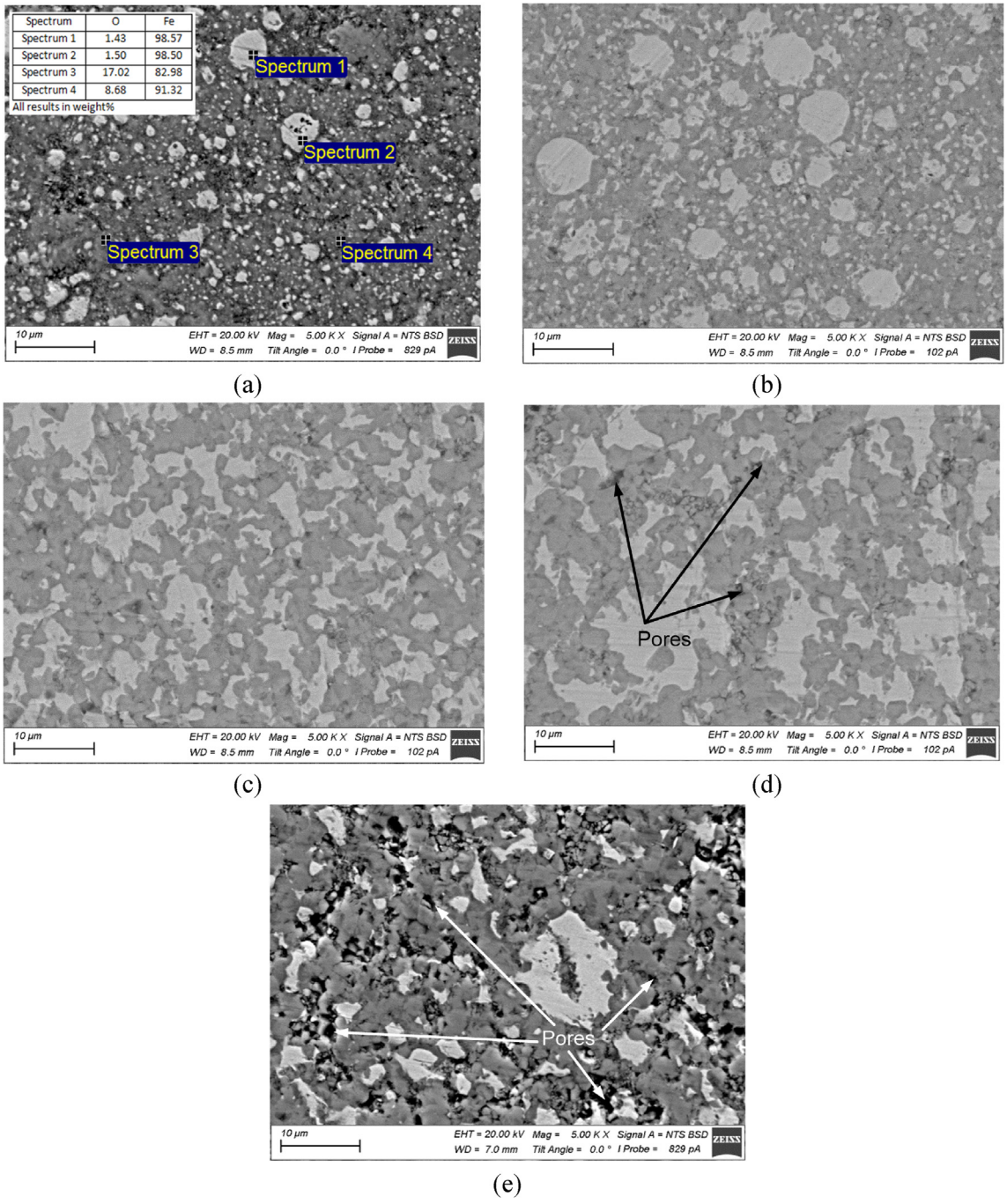

Figure 5. SEM images of a consolidated samples obtained by isostatic pressing followed by sintering at (a) 600 °C, (b) 700 °C, (c) 800 °C, (d) 900 °C and (e) 1000 °C.

exposure time (immersion time) has been found to increase the concentration of ions released. The released ions are non-toxic. As described in [25], ingestion of less than 20 mg/kg of iron is non-toxic A more nuanced examination [26] clearly demonstrates that existing regulatory processes are more than adequate to limit the toxicity of iron even in response to iron overload. Only under pathological or artificially harsh situations of exposure to excess iron (more than 60 mg/kg per ounce) does it become problematic.

The degradation rate was calculated from the concentration of the ions released in Hank's solution after 30 - day testing was 2.27 $g \times m^{-2} \times day^{-1}$ for the Fe - Fe_3O_4 sample, 0.115 $g \times m^{-2} \times day^{-1}$ for the Fe sample. The degradation rate values in Hank's solution calculated for the Fe-Fe_3O_4 sample were 3 times higher than those for the Fe - Fe_2O_3 composite obtained by spark plasma sintering [16], and the concentration of Fe ions released was 10 times higher than that of Fe ions after degradation of the bioresorbable Fe/Mg_2Si composite [27].

Figure 9 shows typical SEM images of the surfaces of Fe (Figure 9 a, b) and Fe - Fe_3O_4 (Figure 9 c, d) samples after 30-day exposure in saline solution (0.9 wt%) as well as corrosion products. It should be noted that no significant differences in the morphology of the corrosion products on the surface were observed. However, upon detailed examination, the surface morphology of the Fe sample (Figure 9 b) was found to be

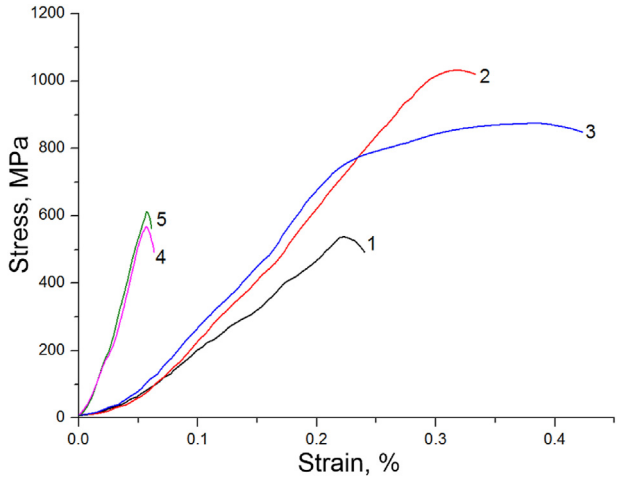

Figure 6. Compressive stress - strain curves obtained by isostatic pressing followed by sintering at 600°C – 1, 700°C – 2, 800°C – 3, 900°C – 4, 1000°C – 5.

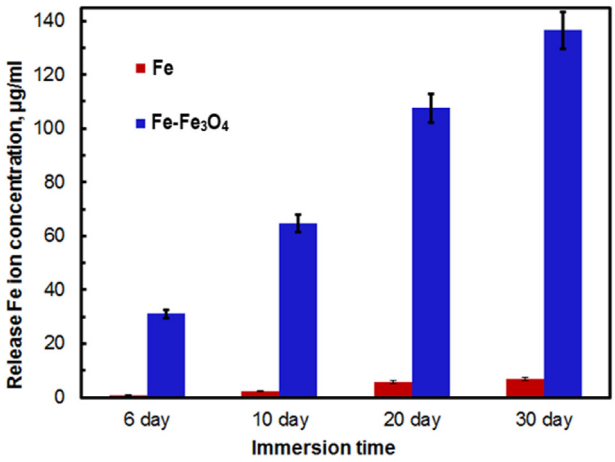

Figure 8. Iron ion concentrations released from experimental Fe - Fe_3O_4 composites and pure iron after immersion in Hank's solution at 37 °C for 6, 10, 20 and 30 days.

represented mainly by large sheets, between which are a large number of spherical particles of the initial iron powder. The deposition of corrosion products in the form of smaller sheets was observed on the surface of the Fe - Fe_3O_4 sample (Figure 9 d), which are macroscopically relatively uniformly distributed over the surface of the sample.

Based on the similarity of the morphology of the sample degradation products, it can be concluded that the corrosion mechanism of Fe - Fe_3O_4 is similar to the mechanism of galvanic corrosion of pure Fe. Cl^- ions present in the corrosive environment displace oxygen from the oxide film, which makes the film soluble. The anodic and cathodic reactions of iron in saline solution can be represented as follows (Eqs. (3), (4)):

$$Fe+2OH^- - 2\bar{e} \rightarrow Fe(OH)_2 \text{ (anode)} \quad (3)$$

$$O_2+2H_2O+4\bar{e} \rightarrow 4OH^- \text{ (cathode)} \quad (4)$$

As corrosion develops, iron hydroxide is formed and the above process is similar to corrosion process in the Fe – Fe_2O_3 system [16]. The presence in the nanoparticles of the second component Fe_3O_4, which is a semiconductor, leads to the accumulation of electrons at the interface and contributes to a growth in corrosion sites at the interfaces in the nanoparticles.

4. Conclusion

Bulk samples with high physical and mechanical characteristics were obtained from Fe - Fe_3O_4 nanopowder by isostatic pressing followed by vacuum sintering. The optimum sintering temperature of nanopowders was found to be 700 °C, providing the highest strength characteristics: ultimate compressive strength was about 1000 MPa due to the processes of coalescence and the small size of the coherent scattering regions D_{CSR}, as well as the high relative density - about 75% of TD. An increase in the sintering temperature has been found to lead to the interaction of Fe with Fe_3O_4 resulting in the formation of FeO and the appearance of large pores, as a result, the samples obtained at 900 °C and 1000 °C have low strength - 580 and 600 MPa, respectively, and are characterized by brittle fracture in tests on compression. Bulk Fe- Fe_3O_4 samples have a high degradation rate, which was 0.62 mm/year in normal saline (0.9% wt. NaCl), which is 7 times higher than that of the bulk samples obtained by sintering Fe nanoparticles under the same conditions.

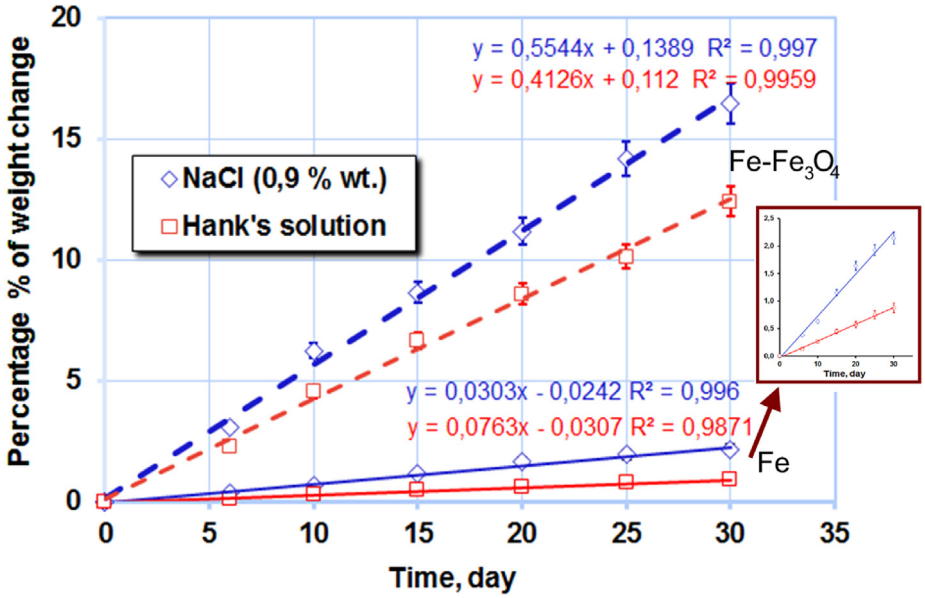

Figure 7. Changes of percentage of Fe and Fe - Fe_3O_4 weight during one-month of immersion at 37 °C in NaCl (0.9 % wt.) and Hank's solution.

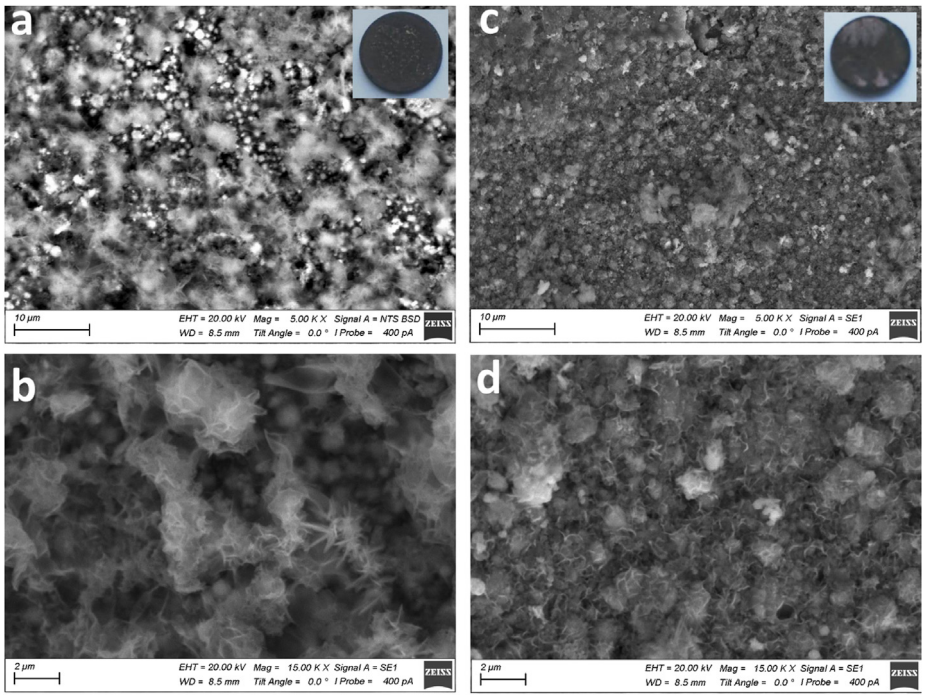

Figure 9. SEM images of the surface of Fe (a, b) and Fe - Fe_3O_4 (c, d) samples after 30 days of exposure in 0.9% NaCl solution with different magnifications.

Declarations

Author contribution statement

Lozhkomoev A. S: Analyzed and interpreted the data; Wrote the paper.

Kazantsev S. O, Bakina O. V, Pervikov A.V, Sharipova A. F: Performed the experiments.

Chymaevskii A. V: Contributed reagents, materials, analysis tools or data.

Lerner M. I: Conceived and designed the experiments.

Funding statement

This work was supported by the Russian Foundation for Basic Research (RFBR) and the Ministry of Science and Technology of Israel (MOST) according to the research project № 19-53-06006 and according to the Government research assignment for ISPMS SB RAS, project FWRW-2022-0002.

Data availability statement

No data was used for the research described in the article.

Declaration of interests statement

The authors declare no conflict of interest.

Additional information

No additional information is available for this paper.

References

[1] C.S. Kumar, G. Singh, S. Poddar, N. Varshney, S.K. Mahto, A.S. Podder, G.S. Mahobia, High-manganese and nitrogen stabilized austenitic stainless steel (Fe–18Cr–22Mn–0.65 N): a material with a bright future for orthopedic implant devices, Biomed. Mater. 16 (6) (2021), 065011.

[2] C. Gao, M. Yao, S. Li, P. Feng, S. Peng, C. Shuai, Highly biodegradable and bioactive Fe-Pd-bredigite biocomposites prepared by selective laser melting, J. Adv. Res. 20 (2019) 91–104.

[3] B. Liu, Y.F. Zheng, Effects of alloying elements (Mn, Co, Al, W, Sn, B, C and S) on biodegradability and in vitro biocompatibility of pure iron, Acta Biomater. Acta Materialia Inc. 7 (3) (2011) 1407–1420.

[4] T. Huang, J. Cheng, D. Bian, Y. Zheng, Fe-Au and Fe-Ag composites as candidates for biodegradable stent materials, J. Biomed. Mater. Res. Part B Appl. Biomater. 104 (2) (2016) 225–240.

[5] M. Schinhammer, A.C. Hänzi, J.F. Löffler, P.J. Uggowitzer, Design strategy for biodegradable Fe-based alloys for medical applications, Acta Biomater. Acta Materialia Inc. 6 (5) (2010) 1705–1713.

[6] A. Purnama, H. Hermawan, J. Couet, D. Mantovani, Assessing the biocompatibility of degradable metallic materials: state-of-the-art and focus on the potential of genetic regulation, Acta Biomater. Acta Materialia Inc. 6 (5) (2010) 1800–1807.

[7] H. Hermawan, H. Alamdari, D. Mantovani, D. Dubé, Iron–manganese: new class of metallic degradable biomaterials prepared by powder metallurgy, Powder Metall. 51 (1) (2008) 38–45.

[8] J. He, F.–L. He, D.-W. Li, Y.-L. Liu, Y.-J. Ye, D.-C. Yin, Advances in Fe-based biodegradable metallic materials, RSC Adv. Royal Society of Chemistry 6 (114) (2016) 112819–112838.

[9] C.S. Obayi, R. Tolouei, A. Mostavan, C. Paternoster, S. Turgeon, B.A. Okorie, D.O. Obikwelu, D. Mantovani, Effect of grain sizes on mechanical properties and biodegradation behavior of pure iron for cardiovascular stent application, Biomatter. Taylor & Francis 2535 (August) (2014) 1–9.

[10] J. Čapek, J. Kubásek, D. Vojtěch, E. Jablonská, J. Lipov, T. Ruml, Microstructural, mechanical, corrosion and cytotoxicity characterization of the hot forged FeMn30(wt.%) alloy, Mater. Sci. Eng. C 58 (2016) 900–908.

[11] B. Liu, Y.F. Zheng, L. Ruan, In vitro investigation of Fe30Mn6Si shape memory alloy as potential biodegradable metallic material, Mater. Lett. Elsevier B.V. 65 (3) (2011) 540–543.

[12] B. Liu, Y.F. Zheng, Effects of alloying elements (Mn, Co, Al, W, Sn, B, C and S) on biodegradability and in vitro biocompatibility of pure iron, Acta Biomater. Acta Materialia Inc. 7 (3) (2011) 1407–1420.

[13] F. Moszner, S.S.A. Gerstl, P.J. Uggowitzer, J.F. Löffler, Structural and chemical characterization of the hardening phase in biodegradable Fe-Mn-Pd maraging steels, J. Mater. Res. 29 (9) (2014) 1069–1076.

[14] F. Moszner, E. Povoden-Karadeniz, S. Pogatscher, P.J. Uggowitzer, Y. Estrin, S.S.A. Gerstl, E. Kozeschnik, J.F. Löffler, Reverse $\alpha' \rightarrow \gamma$ transformation mechanisms of martensitic Fe-Mn and age-hardenable Fe-Mn-Pd alloys upon fast and slow continuous heating, Acta Mater. 72 (2014) 99–109.

[15] J. Cheng, Y.F. Zheng, In vitro study on newly designed biodegradable Fe-X composites (X = W, CNT) prepared by spark plasma sintering, J. Biomed. Mater. Res. Part B Appl. Biomater. 101 (4) (2013) 485–497.

[16] J. Cheng, T. Huang, Y.F. Zheng, Microstructure, mechanical property, biodegradation behavior, and biocompatibility of biodegradable Fe-Fe2O3 composites, J. Biomed. Mater. Res., Part A 102 (7) (2014) 2277–2287.

[17] A. Sharipova, V. Slesarenko, E. Gutmanas, Synthesis of metal-metal oxide (Me-MenOm) nanocomposites by partial reduction and cold sintering, Mater. Lett. 276 (2020), 128197.

[18] A.S. Lozhkomoev, A.V. Pervikov, S.O. Kazantsev, A.F. Sharipova, N.G. Rodkevich, N.E. Toropkov, M.I. Lerner, Synthesis of Fe/Fe3O4 core-shell nanoparticles by electrical explosion of the iron wire in an oxygen-containing atmosphere, J. Nanoparticle Res. 23 (3) (2021) 1–12.
[19] Y.A. Kotov, Electric explosion of wires as a method for preparation of nanopowders, J. Nanoparticle Res. 5 (2003) 539–550.
[20] M.I. Lerner, A.V. Pervikov, E.A. Glazkova, N.V. Svarovskaya, A.S. Lozhkomoev, S.G. Psakhie, Structures of binary metallic nanoparticles produced by electrical explosion of two wires from immiscible elements, Powder Technol. 288 (2016) 371–378.
[21] Marat I. Lerner, ElenaA. Glazkova, Aleksandr S. Lozhkomoev, et al., Synthesis of Al nanoparticles and Al/AlN composite nanoparticles byelectrical explosion of aluminum wires in argon and nitrogen, Powder Technol. 295 (2016) 307–314.
[22] W. Du, et al., Effects of trace Ca/Sn addition on corrosion behaviors of biodegradable Mg–4Zn–0.2 Mn alloy, J. Magnesium Alloys 6 (1C) (2018) 1–14.
[23] E.Y. Gutmanas, L.I. Trusov, I. Gotman, Consolidation, microstructure and mechanical properties of nanocrystalline metal powders, Nanostruct. Mater. 4 (8) (1994) 893–901.
[24] Y. Yang, et al., In-situ deposition of apatite layer to protect Mg-based composite fabricated via laser additive manufacturing, J. Magnesium Alloys (2021). In press.
[25] H.W. Yuen, W. Becker, Iron Toxicity//StatPearls [Internet], StatPearls Publishing, 2021.
[26] R. Eid, N.T.T. Arab, M.T. Greenwood, Iron mediated toxicity and programmed cell death: a review and a re-examination of existing paradigms, Biochim. Biophys. Acta Mol. Cell Res. 1864 (2C) (2017) 399–430.
[27] M. Sikora-Jasinska, et al., Long-term in vitro degradation behaviour of Fe and Fe/Mg2Si composites for biodegradable implant applications, RSC Adv. 8 (18C) (2018) 9627–9639.